

Lu, X., Zhang, W., Tseng, Y., Liu, R., Tao, Z., Paris, E., ... Schmitt, T. (2022). Spin-excitation anisotropy in the nematic state of detwinned FeSe. *Nature Physics*, 18(7), 806–812. <https://doi.org/10.1038/s41567-022-01603-1>

Spin-excitation anisotropy in the nematic state of detwinned FeSe

Xingye Lu,^{1,*} Wenliang Zhang,² Yi Tseng,² Ruixian Liu,¹ Zhen Tao,¹ Eugenio Paris,² Panpan Liu,¹ Tong Chen,³ Vladimir N. Strocov,² Yu Song,⁴ Rong Yu,⁵ Qimiao Si,³ Pengcheng Dai,^{3,†} and Thorsten Schmitt^{2,‡}

¹ *Center for Advanced Quantum Studies, Applied Optics Beijing Area Major Laboratory, and Department of Physics, Beijing Normal University, Beijing 100875, China*

² *Photon Science Division, Swiss Light Source, Paul Scherrer Institut, CH-5232 Villigen PSI, Switzerland*

³ *Department of Physics and Astronomy, Rice Center for Quantum Materials, Rice University, Houston, TX 77005, USA*

⁴ *Center for Correlated Matter and Department of Physics, Zhejiang University, Hangzhou 310058, China*

⁵ *Department of Physics, Renmin University of China, Beijing 100872, China*

The origin of the electronic nematicity in FeSe is one of the most important unresolved puzzles in the study of iron-based superconductors. In both spin- and orbital-nematic models, the intrinsic magnetic excitations at $\mathbf{Q}_1 = (1, 0)$ and $\mathbf{Q}_2 = (0, 1)$ of twin-free FeSe are expected to provide decisive criteria for clarifying this issue. Although a spin-fluctuation anisotropy below 10 meV between \mathbf{Q}_1 and \mathbf{Q}_2 has been observed by inelastic neutron scattering at low temperature, it remains unclear whether such an anisotropy also persists at higher energies and associates with the nematic transition T_s . Here we use resonant inelastic x-ray scattering to probe the high-energy magnetic excitations of detwinned FeSe. A prominent anisotropy between the magnetic excitations along the H and K directions is found to persist to $E \approx 200\text{meV}$, which decreases gradually with increasing temperature and finally vanishes at a temperature around T_s . The measured high-energy spin excitations are dispersive and underdamped, which can be understood from a local-moment perspective. Taking together the large energy scale far beyond the d_{xz}/d_{yz} orbital splitting, we suggest that the nematicity in FeSe is likely spin-driven.

Intertwined order and fluctuations in high-transition-temperature (T_c) superconductors are pivotal for understanding the microscopic origin of superconducting electron pairing¹. Of particular interest is the electronic nematic state present in both cuprate and iron-based superconductors (FeSCs). Initially discovered through in-plane electronic anisotropy with C_2 symmetry in the paramagnetic orthorhombic state of detwinned $\text{Ba}(\text{Fe}_{1-x}\text{Co}_x)_2\text{As}_2$ (refs. ²⁻⁴), the electronic nematic state (and its fluctuations) has been identified as a ubiquitous feature of FeSCs and is believed to be essential for the structural and magnetic transitions in FeSCs (refs. ⁵⁻⁹), and may enhance the electron pairing for high- T_c superconductivity¹⁰⁻¹².

Iron selenide (FeSe) is a unique material among FeSCs because of its simple structure (Fig. 1a)¹³ and unusual electronic properties, such as strong anisotropy of the superconducting order parameter, extended electronic nematic phase and highly tunable T_c (ref. ⁹). In particular, unlike iron pnictide, which has a collinear antiferromagnetic (AF) ground state below the tetragonal-to-orthorhombic structural (nematic) phase transition T_s , although FeSe exhibits a similar nematic transition ($T_s \approx 90\text{ K}$)¹⁴, it has no static AF order, providing a broad temperature range below T_s as an ideal platform for investigating electronic nematicity and its interplay with superconductivity.

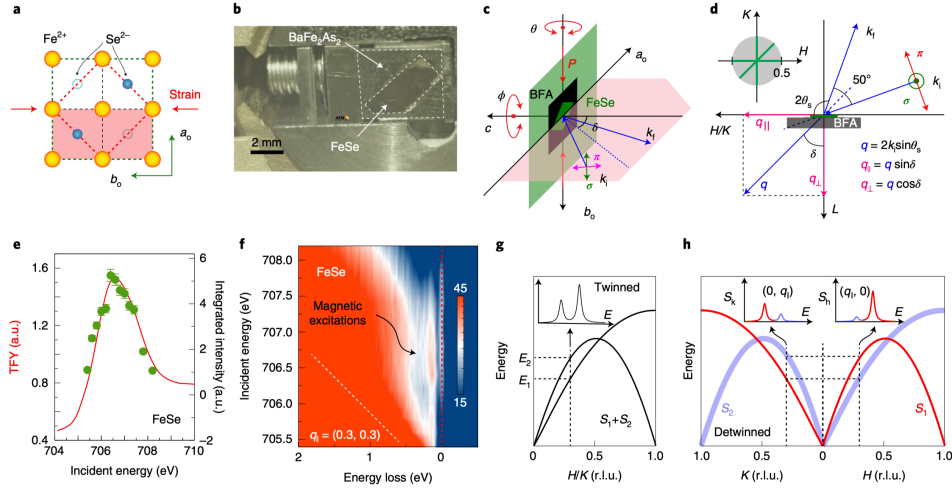


Fig. 1 Crystal structure, detwinning strategy, scattering geometry and incident energy-dependent RIXS. **a**, Structure of the FeSe layer. The FeSe crystal consists of stacked FeSe layers. The yellow-filled circles represent Fe^{2+} ions. The filled and open blue circles denote Se^{2-} ions above and below the Fe-Fe plane, respectively. The horizontal arrows mark the direction of the uniaxial strain. The red dashed diamond and green dashed square denote the tetragonal and orthorhombic unit cells, respectively. **b**, A mechanical detwinning device installed on the RIXS spectrometer, with a thin FeSe crystal glued on a pre-cleaved BaFe_2As_2 crystal that is pressured in the device. **c,d**, Scattering geometry for RIXS measurements. \mathbf{q}_{\parallel} and \mathbf{q}_{\perp} are projections of \mathbf{q} onto $[H, K]$ plane and L direction. The sample rotation θ around the vertical axis controls the in-plane momentum transfer \mathbf{q}_{\parallel} and the rotation ϕ around the c axis can tune the scattering plane (pink area) (**c**). The grey-filled circle in **d** marks the momentum area accessible in this study ($|\mathbf{q}_{\parallel}| \lesssim 0.5$). The green lines in the grey area in **d** show the high-symmetry directions for RIXS measurements. P denotes uniaxial pressure; $k_{i/f}$, initial/final wave vector of photon; and BFA, BaFe_2As_2 . **e**, The red curve is the total fluorescence yield (TFY) XAS spectrum of FeSe collected near the Fe- L_3 edge (left axis). The green-filled circles represent the integrated intensity (right axis) of the magnetic excitations shown in **f**. The error bars in **e** are estimated from the statistics of the data and the 95% confidence interval of the fittings. **f**, Incident-energy dependence of the excitations of FeSe at $\mathbf{q}_{\parallel} = (0.3, 0.3)$, measured near the Fe- L_3 edge with π polarization at $T = 20$ K. The magnetic excitations are marked by a curved arrow. **g,h**, Schematics of magnetic excitation dispersions for twinned (**g**) and detwinned (**h**) FeSe assuming a difference between spin excitations S_2 and S_1 . Correspondingly, the insets in **g** and **h** show schematic RIXS energy spectra for twinned and detwinned FeSe.

FeSe consists of stacked charge-neutral FeSe layers (Fig. 1a). On cooling, it undergoes a nematic transition at $T_s \approx 90$ K, below which twin domains form along two mutually perpendicular directions and exhibit macroscopic four-fold symmetry, impeding the study of the intrinsic electronic properties of the orthorhombic (nematic) state. Through detwinning of FeSe using uniaxial strain, resistivity and electronic structure measurements reveal strong electronic anisotropy in the nematic state^{15,16}. At lower temperature, FeSe enters a superconducting ground state with $T_c \approx 9$ K, in which a superconducting energy gap anisotropy has been observed via angle-resolved photoemission spectroscopy (ARPES)^{17–19} and scanning tunnelling spectroscopy²⁰.

In the presence of orbital splitting (or orbital ordering) between d_{xz} and d_{yz} orbitals^{16,21,22}, and the absence of magnetic order, the electronic nematic phase has been suggested to be driven by orbital fluctuations^{23–26}. On the other hand, experimental evidence, in particular the discovery of intense magnetic excitations and their correlation with the nematic transition^{27–29}, has emphasized the importance of the spin degree of freedom in driving electronic nematic order. In addition, various localized models based on quantum paramagnetism, spin frustration and magnetic quadrupolar order have been proposed to account for the nematic transition, magnetic excitations and the absence of AF

order^{30–33}.

It is proposed that resolving the intrinsic magnetic excitations in twin-free FeSe is key to clarifying the microscopic origin of the unusual electronic anisotropy in both the superconducting and nematic states^{5,6,34}. By employing BaFe₂As₂ as a substrate for applying uniaxial strain, some of us have recently measured low-energy spin fluctuations ($E \lesssim 10$ meV) of detwinned FeSe using inelastic neutron scattering³⁵. These results have revealed anisotropic spin fluctuations in the normal state and a spin resonance appearing only at $\mathbf{Q}_1 = (1, 0)$ below T_c , consistent with the picture of orbital-selective Cooper pairing^{20,36–38}. However, neutron scattering experiments were unable to determine what happens to the magnetic excitation anisotropy across the nematic transition due to enhanced background scattering from the large aluminium detwinning device on warming to T_s . In addition, the energy scale of the magnetic anisotropy is unknown because the background magnetic scattering from the BaFe₂As₂ substrate overwhelms the magnetic signal from FeSe for energies above 10 meV (ref. ³⁵).

An ideal method to probe the intrinsic magnetic excitations of FeSe is resonant inelastic X-ray scattering (RIXS) at the Fe-L₃ edge in combination with the aforementioned detwinning method (Fig. 1b)^{39–44}. RIXS at transition-metal L edges has been widely used to study the (para)magnons of cuprate and FeSCs, as well as various elementary excitations including phonons, crystal-field excitations and plasmons^{39–49}. Because Fe-L₃ X-rays (707 eV) penetrate less than 100 nm into FeSe, but the typical thickness of a cleaved FeSe single crystal is ~ 20 μm , RIXS studies of FeSe are free from signal contamination due to BaFe₂As₂ and provide a unique opportunity for measuring high-energy magnetic excitations on detwinned FeSe with high efficiency.

In this Article we use RIXS to measure the intrinsic spin excitations of FeSe and BaFe₂As₂ along the high-symmetry directions H , K and $[H, H]$, denoted by $S_h(q_{\parallel})$, $S_k(q_{\parallel})$ and $S_{hh}(q_{\parallel})$, respectively (Figs. 2 and 3). To facilitate discussions, we define the spin excitations associated with $\mathbf{Q}_1 = (1, 0)$ as $S_1(\mathbf{q}, E)$ and those associated with $\mathbf{Q}_2 = (0, 1)$ as $S_2(\mathbf{q}, E)$. The ratio between $S_h(q_{\parallel})$ and $S_k(q_{\parallel})$, $\psi(q_{\parallel}) = S_h(q_{\parallel})/S_k(q_{\parallel})$, directly probes the spin-excitation unbalance between S_1 and S_2 , which is commonly referred to as nematic spin correlations in the nematic ordering and fluctuating region^{34,50,51}. We denote the momentum transfer in reciprocal lattice units (r.l.u.; see Experimental set-ups in the Methods).

Our results reveal that the spin-excitation anisotropy in detwinned FeSe manifests over a large energy range up to 200 meV. It persists up to a temperature slightly above T_s , before fading away at a temperature well above T_s . Its comparison with the intrinsic spin-wave anisotropy of BaFe₂As₂ establishes strong nematic spin correlations in both energy scale and amplitude in FeSe. This strong spin-excitation anisotropy builds a direct connection with the nematic phase, suggesting that the nematic order is primarily spin-driven because the energy range of the nematic-phase-induced spin-excitation anisotropy is much larger than that of orbital splitting^{22–24}. Furthermore, the RIXS results identify dispersive high-energy spin excitations that are underdamped, which is highly peculiar for a paramagnet, but can be understood from a local-moment-based model with antiferroquadrupolar (AFQ) order³¹. As such, our results provide much-needed new insights into the mechanism for the nematicity of FeSe.

Figure 1b shows an FeSe crystal that has been prepared for RIXS measurements, and is glued onto

a square-shaped BaFe_2As_2 sample with the same orientation. Uniaxial pressure is applied on the BaFe_2As_2 along the tetragonal $[110]$ direction (orthorhombic b axis). On cooling, the BaFe_2As_2 will be detwinned below $T_s \approx 138$ K and generates an orthorhombic distortion $\delta = (a - b)/(a + b) = 0.36\%$ that can be transferred to and thereby detwin FeSe below its structural transition at $T_s \approx 90$ K. Figure 1c,d illustrates the scattering geometry, the substantial area of the first Brillouin zone accessible with Fe- L_3 RIXS, and calculations of the in-plane momenta q_{\parallel} .

We first carried out incident-energy-dependent RIXS (energy detuning) measurements for both BaFe_2As_2 and FeSe around their resonating energies, which were determined by X-ray absorption spectroscopy (XAS; Fig. 1e and Supplementary Fig. 2). Figure 1f presents a RIXS map for an unstrained FeSe sample measured at $\mathbf{q}_{\parallel} = (0.3, 0.3)$ with π polarization and $T = 20$ K. Although fluorescence and particle-hole excitations dominate the scattering signal above $E \approx 0.5$ eV, a clear intrinsic elementary excitation (Raman mode) is observed at $E \approx 160$ meV that is well separated from the fluorescence peak setting above $E \approx 200$ meV. The integrated intensity of this Raman mode (Fig. 1e, green circles) follows the XAS (Fig. 1e, red curve), indicating that the cross-section is enhanced near the Fe- L_3 edge. In addition, phonon contributions to this mode can also be excluded because of their much smaller energy scale ($E \approx 40$ meV)⁴³. Taking together the consistency in energy dispersion between the excitations in Figs. 2 and 3 and those reported in previous studies^{39,43,44}, we can safely attribute these dispersive excitations to single spin-flip magnetic excitations.

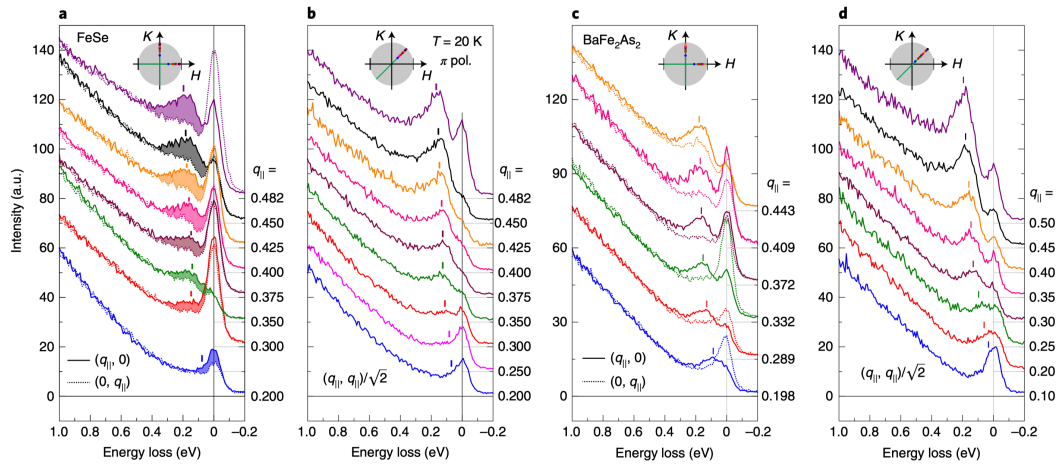


Fig. 2 Summary of RIXS results on detwinned FeSe and BaFe_2As_2 . a,b, Momentum-dependent RIXS spectra of FeSe along the H (solid lines) (a) and K (dashed lines) directions (a) and twinned FeSe along the $[H, H]$ direction (b). The shaded areas mark the difference between $S_h(q_{\parallel})$ and $S_k(q_{\parallel})$. c,d, Momentum-dependent RIXS spectra of detwinned BaFe_2As_2 along the H/K (c) and $[H, H]$ (d) directions. The coloured dots in the insets mark the momenta where spectra were collected.

To quantitatively determine the spin-excitation anisotropy in FeSe, we measured the spin excitations of both detwinned FeSe and BaFe_2As_2 samples (Figs. 2 and 3), taking the latter as a reference; this can be compared to previous neutron scattering studies of detwinned BaFe_2As_2 (ref.⁵⁰). Before discussing the results, we illustrate in Fig. 1g,h the principle for resolving the inherent spin-wave anisotropy and nematic spin correlations in the first Brillouin zone (Supplementary Fig. 3). In a twinned sample with anisotropic excitations, RIXS measurements generate $S_h = S_k$ (black curve in the inset of

Fig. 1g). Both S_h and S_k consist of two spin-excitation branches from S_1 and S_2 in twin domains, where we assume S_1 and S_2 have the same energy dispersion for simplicity. For a detwinned sample with local-moment AF order, the spin waves emanate only from the AF vector $\mathbf{Q}_1 = (1, 0)$ ($S_2 = 0$), and S_h/S_k determines the inherent spin-wave anisotropy of S_1 . In a detwinned system with nematic spin correlations ($S_1 \neq S_2 \neq 0$), S_1 and S_2 will be present along both H and K directions (Fig. 1h) with different spectral weights, for which the ratio between S_h and S_k reflects the nematic spin correlations (Supplementary Fig. 3).

Momentum-dependent RIXS spectra of FeSe and BaFe₂As₂ collected at $T = 20 \text{ K} < T_s$ are summarized in Fig. 2. In both samples, highly dispersive magnetic excitations along three high-symmetry directions H , K and $[H, H]$ are resolved. Figure 2a (2c) displays the intrinsic spin excitations of FeSe (BaFe₂As₂) along the H and K directions, and Fig. 2b (2d) along the $[H, H]$ direction. Although twinned FeSe and BaFe₂As₂ are expected to show four-fold symmetric magnetic excitations^{39,52} [$S_h(q_{\parallel}) = S_k(q_{\parallel})$], we find that the detwinned samples exhibit highly anisotropic excitations with $S_h(q_{\parallel}) > S_k(q_{\parallel})$. The substantial difference between $S_h(q_{\parallel})$ and $S_k(q_{\parallel})$ for FeSe persists at all q_{\parallel} measured (Fig. 2a, shaded areas), thus demonstrating the existence of a high-energy spin-excitation anisotropy (nematic spin correlations) in the nematic state of detwinned FeSe. For BaFe₂As₂, the spin-excitation anisotropy is a manifestation of the inherent difference in the spin-wave branches along the H and K directions⁵⁰. The spin-wave anisotropy of BaFe₂As₂ increases with q_{\parallel} up to 0.409 but decreases at higher $q_{\parallel} = 0.443$ (Fig. 2c), revealing a non-monotonic momentum dependence. In comparison, the spectral weight difference in FeSe (Fig. 2a, shaded area) retains a large amplitude at an even higher $q_{\parallel} = 0.482$.

To achieve a quantitative characterization of the spin-excitation anisotropy in FeSe and BaFe₂As₂, we use a general damped harmonic oscillator model^{39-41,43}

$$S(q, E) = A \frac{E_0}{1 - e^{-\beta E}} \frac{2\gamma E}{(E^2 - E_0^2)^2 + (\gamma E)^2} \quad (1)$$

to fit the magnetic excitations, in which E_0 is the undamped energy, γ the damping factor, $\beta = \frac{1}{k_B T}$ (k_B is the Boltzmann constant) and A is a fitting coefficient. The elastic peak can be fitted with a Gaussian function, and the fluorescence contributions below $E \approx 1 \text{ eV}$ can be described with a quadratic polynomial (Supplementary Figs. 5 and 6).

The fitting results for FeSe and BaFe₂As₂, the undamped energy dispersion ($E_0(q)$), the energies for the intensity maxima ($E_m(q)$) and the damping factor ($\gamma/2$) are summarized in Fig. 3. Figure 3a-c shows a simulation of the spin waves in BaFe₂As₂ overlaid by the energy dispersions and the damping factors. The simulation is based on an anisotropic Heisenberg $J_{1a}-J_{1b}-J_2$ model as described in ref. ⁵² (J_{1a} (J_{1b}) is the nearest-neighbour exchange interaction along a (b) axis. J_2 is the next-nearest-neighbour exchange interaction.), in which we set $L = 0$ because the spin waves of BaFe₂As₂ are two-dimensional, especially for the high-energy spin excitations probed in our RIXS measurements. We find $E_0 > \gamma/2$ at all the momenta measured, which indicates that the spin waves are underdamped and far from being critically damped. The intrinsic spin waves of the clearly resolved two different branches $S_h(q)$ and $S_k(q)$

around Γ are consistent with the anisotropic Heisenberg model, in which dispersive spin waves can only arise from the AF wave vector \mathbf{Q}_1 (S_1). The minor deviation of the branch $S_k(q)$ from the anisotropic Heisenberg model can be attributed to the failure of the anisotropic Heisenberg model in describing the small anisotropy of magnetic excitations at high energy, due to the emergence of the spin excitations around $\mathbf{Q}_2 = (0, 1)$ (S_2) at $E \gtrsim 100$ meV observed by neutron scattering^{50,51}. Figure 3d shows the energy dispersion of FeSe obtained from the fitting of the magnetic excitations shown in Fig. 2a,b. The filled symbols mark the bare energy dispersion (E_0) without damping effect, and the open symbols represent the energy dispersion for the intensity maxima E_m .

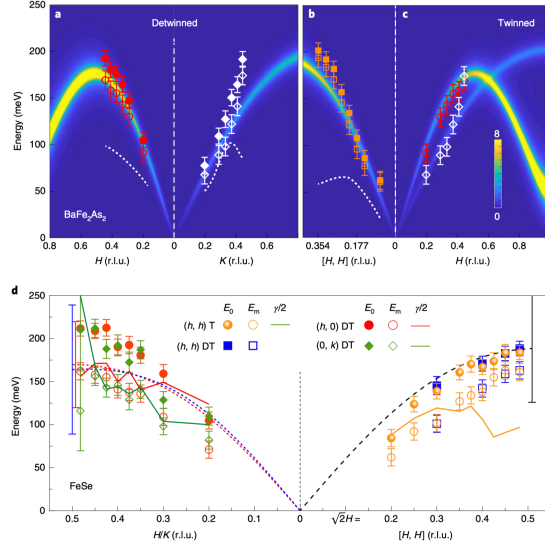


Fig. 3 Energy dispersions and damping factors for the magnetic excitations of FeSe and BaFe₂As₂. a-c, Comparison between dispersions of the magnetic excitations measured with RIXS and a simulation with a Heisenberg model for detwinned (a) and twinned (b,c) BaFe₂As₂ (ref.⁵²). The filled symbols, open symbols and white dashed curves in a and b are undamped energies (E_0), energies for the intensity maxima (E_m) and the damping factor ($\gamma/2$) fitted from the spectra shown in Fig. 2c,d with equation (1). The open symbols in c show E_m . d, Spin-excitation energy dispersions of FeSe obtained from the fitting of the RIXS spectra in Fig. 2a,b with equation (1). The filled (open) red circles, green diamonds, orange circles, and blue squares mark the undamped energies E_0 (energies for intensity maxima E_m) of the dispersions along H (detwinned, DT), K (detwinned), $[H, H]$ (twinned, T) and $[H, H]$ (detwinned) directions, respectively. The red, green, and orange lines mark the momentum-dependent damping factor $\gamma/2$ along the high-symmetry directions. The black, red, and blue dashed curves are the calculated flavor-wave dispersions in the AFQ phase along the $[H, H]$, and H/K directions, respectively. The error bars for the data points are estimated according to the confidence interval of the fittings and the error in determining the $E = 0$ position. The error bars mark the damping factor $\gamma/2$ along the corresponding directions.

The momentum-dependent damping factors $\gamma/2$ are overall larger than that for BaFe₂As₂, but still in the underdamped regime for most of the excitations. Moreover, the damping factor for S_{hh} (along the $[H, H]$ direction) is smaller than for S_{hk} in both FeSe and BaFe₂As₂, suggesting a common anisotropic damping effect in FeSC. The (anisotropic) underdamped nature of the magnetic excitations, not inferable in previous neutron scattering and RIXS studies on twinned samples^{28,43}, suggests that the excitations should arise from interacting local moments associated with strong electron correlations⁵³.

Because the largest momentum (0.482, 0) along H is close to the zone boundary (0.5, 0), the excitation energy scale of FeSe ($E_0 \approx 200$ meV and $E_m \approx 160$ meV) at (0.482, 0) and (0, 0.482) (consistent with that in ref.⁴³) reveals a much higher band top in the first Brillouin zone than that ($E \approx$

120–150 meV) observed by neutron scattering in the Brillouin zone around $(1, 0)$ ²⁸. This is in stark contrast to the case of BaFe_2As_2 , where the dispersions measured by RIXS and neutron scattering can be consistently described with one model (Fig. 3)^{39,50}. We attribute this difference to the absence of stripe AF order in FeSe. Because of the translational symmetry of the stripe AF order ($\mathbf{k} = (1, 0)$) in BaFe_2As_2 , the magnetic excitations in the first Brillouin zone can be deemed as a replica of the ones in the Brillouin zone centring at $Q = (1, 0)$. However, long-range AF order is not established in spite of the strong in-plane magnetic correlations in FeSe. Accordingly, the dispersions around Γ and $(1, 0)$ do not have to be identical. However, how to quantitatively reconcile the neutron scattering and RIXS results is still an open question.

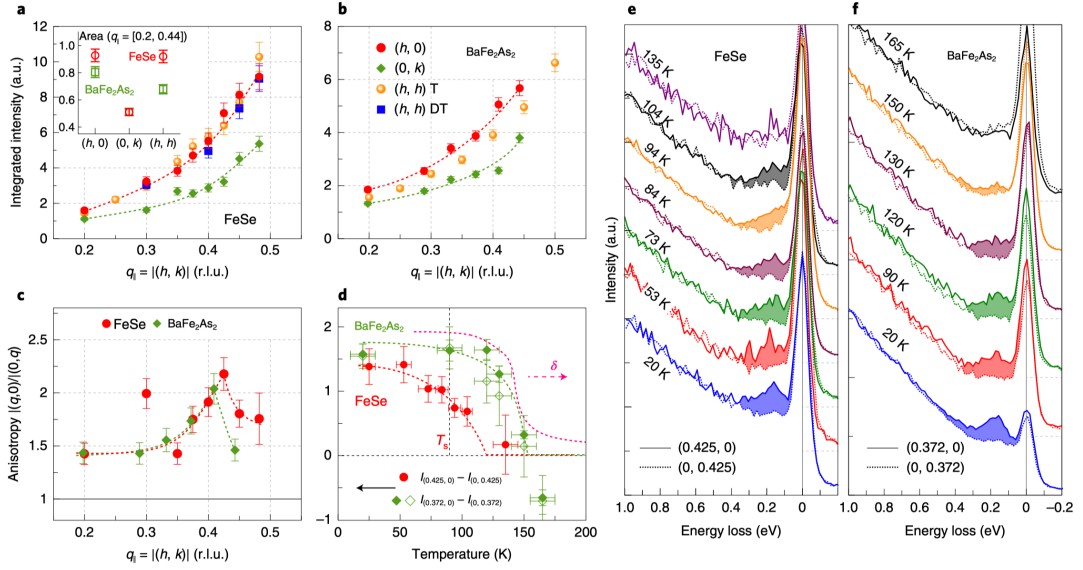


Fig. 4 Anisotropic magnetic excitations in detwinned FeSe and BaFe_2As_2 . **a,b**, Momentum-dependent energy-integrated intensity of magnetic excitations for FeSe (**a**) and BaFe_2As_2 (**b**). The inset shows the momentum-integrated intensity of $S_{h/k/hh}$ for FeSe (red circles) and BaFe_2As_2 (green squares) in the range of $q_{\parallel} = [0.2, 0.44]$. **c**, Spin excitation anisotropy between S_h and S_k , defined as the ratio between the integrated intensity for $(q, 0)$ and $(0, q)$ as shown in **a** and **b**. **d**, Temperature dependence of the spin-excitation difference between $S_h(q_{\parallel})$ and $S_k(q_{\parallel})$, in which the data points are the integrated intensity of $S_h(q_{\parallel}) - S_k(q_{\parallel})$ in the energy range of $[0.08, 0.4]$ eV, as shown in **e** and **f**. The dashed red and green lines in **c** and **d** are guides to the eye. The pink dashed curve shows the lattice distortion $\delta = (a-b)/(a+b)$ of BaFe_2As_2 under a uniaxial pressure of $P \sim 20$ MPa, which reaches 0.36% below $T \sim 100$ K. The vertical black dashed line marks the $T_s = 90$ K for FeSe. The vertical error bars in **a-d** are estimated from the data statistics and the confidence interval of the fittings, which determine the error bars in **c**. The horizontal bars in **d** mark the temperature range where data were collected. **e,f**, Temperature-dependent RIXS spectra for FeSe and BaFe_2As_2 measured at $q_{\parallel} = 0.425$ and 0.372 , respectively. The shaded areas in **e** and **f** mark the intensity difference between $S_h(q_{\parallel})$ and $S_k(q_{\parallel})$.

Figure 4a,b shows the momentum-dependent energy-integrated intensity of the spin excitations S_h , S_k and S_{hh} for FeSe and BaFe_2As_2 , respectively. With increasing q_{\parallel} , the integrated intensities along all three high-symmetry directions increase monotonically. The spin-excitation intensity for FeSe is slightly higher than for BaFe_2As_2 , qualitatively consistent with previous neutron scattering results²⁸. Note that the momentum-direction dependence of the amplitude for $S_{h/k/hh}$ is modulated by the anisotropic damping factor inherent to $S_{1,2}$, which requires $S_{1,2} = 0$ at Γ (ref. 52). To quantify the spin-excitation anisotropy, we plotted the ratio $I(q, 0)/I(0, q) = S_h/S_k$ for FeSe and BaFe_2As_2 in the same panel (Fig. 4c). It is surprising that the spin-excitation anisotropy of FeSe (reflecting the nematic spin

correlations) is rather similar to the spin-wave anisotropy of BaFe_2As_2 in both amplitude and energy scale. Furthermore, in the high-energy/momentum region, the anisotropy of FeSe is even larger than for BaFe_2As_2 . This prominent spin-excitation anisotropy signifies strong electronic nematicity with large energy scale ($E \approx 200$ meV) and magnitude in FeSe. Moreover, the temperature dependence of the difference between S_h and S_k for FeSe at selected $q_{\parallel} = 0.425$ decreases with increasing temperature, persists to a temperature (104 K) 20% higher than T_s and finally drastically reduces at a temperature (135 K) well above T_s , indicating a gradual suppression of nematic spin correlations above T_s (Fig. 4d,e). Because FeSe is under uniaxial strain applied from the BaFe_2As_2 substrate (pink dashed curve, Fig. 4d), T_s is no longer well defined. For this reason, it is not surprising that the spin-excitation anisotropy disappears at a temperature above the zero-pressure T_s . This temperature dependence is similar to that for BaFe_2As_2 , as shown in Fig. 4d,f, where the anisotropy at $q_{\parallel} = 0.372$ persists at a temperature slightly higher than T_N but vanishes at $T = 165$ K.

Previous measurements of the spin dynamics in detwinned FeSe were constrained to low energies ($E \lesssim 10$ meV)³⁵ and were unable to discriminate between the different scenarios for the nematicity in FeSe. Our present measurements over a large energy window enable the discovery that the detwinned FeSe harbours high-energy (up to 200 meV) anisotropic spin excitations that are dispersive and underdamped. This surprising finding appears to be at variance with the itinerant mechanism for the nematicity in FeSe. In the itinerant picture, the leading contribution to the spin excitation spectrum comes from a two-particle process, that is, a convolution of single-electron and single-hole excitations. Because of this particle-hole nature of the spin excitations, damping already appears in the leading-order contribution to the spectrum. This Landau damping means that the leading-order contribution to the spin excitations is generically already overdamped; higher-order processes further enhance the damping. An itinerant model calculation indeed shows that the spin excitations at such pertinent (high) energies are highly overdamped⁵⁴. Our work is expected to motivate further studies on this issue within the itinerant description.

Instead, the dispersive and underdamped nature of the high-energy spin excitations point to a local-moment starting point to describe the nematicity. Taking together that the energy scale of the spin-excitation anisotropy is far beyond the d_{xz}/d_{yz} orbital splitting ($E \approx 50$ meV), and the nematic spin correlations decrease and finally disappear at a temperature above T_s , we conclude that the nematicity is probably spin-driven.

This has led us to consider a generalized bilinear-biquadratic model on a square lattice with local moments³¹. Here, the local moments capture the majority of the spin degrees of freedom, especially at high energies. Indeed, the importance of electron correlations in iron-based superconductors has been clearly demonstrated in recent years. Although several specific theoretical approaches have been taken to address the effect of electron correlations, including Hund's metal⁵⁵, proximity to an orbital-selective Mott phase^{6,56} and a Mott–Hund's picture⁵⁷, they share the common feature that the single-electron states have a mixture of incoherent and coherent states (which dominate at high and low energies, respectively). Indeed, for FeSe, ARPES has directly observed the high-energy Hubbard bands^{58,59}, which mediate effective exchange interactions between quasi-localized moments⁶⁰.

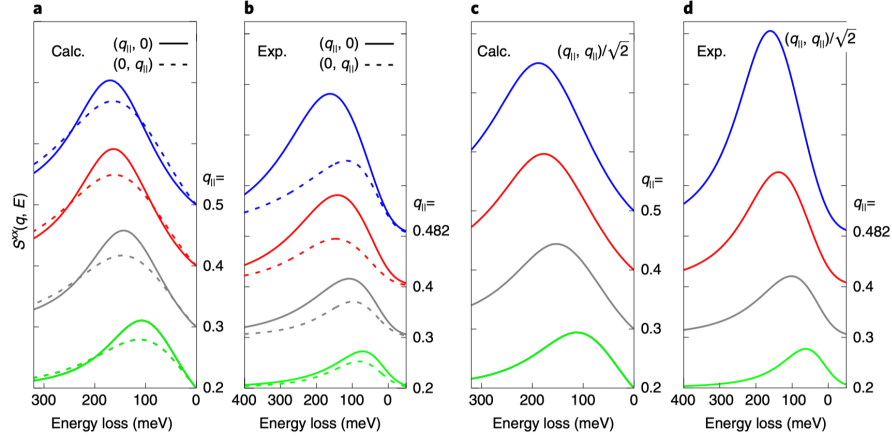


Fig. 5 Calculated spin excitation spectra of the AFQ phase and their comparison with the fitting curve of the experimental $S(\mathbf{q})$ from RIXS. **a,c**, Calculated spectra along the H/K directions (**a**) and the $[H, H]$ direction (**c**). **b,d**, Fitting curves of the experimental $S(q_{||})$ along the H/K directions (**b**) and $[H, H]$ direction (**d**).

In the generalized bilinear-biquadratic model, the leading-order contributions to the spin excitation spectrum comprise a one-particle process. Because only sub-leading contributions that involve more-than-one-particle processes contribute to damping, the high-energy spin excitations are underdamped. More specifically, we have calculated the spin dynamics in the proposed picture for the nematicity based on a $(1, 0)$ antiferroquadrupolar state using the flavor-wave method³¹. This approach treats the spin dipolar and quadrupolar excitations on an equal footing, as the bosonic flavor waves. Consistent with the physical picture, the spin-excitation spectrum is dispersive and underdamped (for details see the Supplementary Information). In Fig. 5 we show that the calculated spin dynamics provide a good understanding of the experimental data. Thus, our results provide evidence for a local-moment-based picture for the nematicity of FeSe.

The rich properties of the Fe-based superconductors in general and nematic FeSe in particular have been addressed from both weak^{5,37,61} and strong^{6,30,31} coupling perspectives, with each having had successes. Our work brings about a hitherto unknown and remarkable feature of universality across Fe-based superconductors. For BaFe_2As_2 with collinear AF order, the anisotropy can be readily interpreted in the picture of intrinsic spin waves^{50,51}. FeSe, by contrast, lacks long-range magnetic order even though it is nematic. The local-moment-based understanding, as dictated by the qualitative similarities in the high-energy spin excitations of FeSe and BaFe_2As_2 , suggests that the largest spin spectral weight in both the iron chalcogenides and pnictides is associated with the incoherent electronic excitations induced by the underlying electron correlations. As such, our work not only allows for discriminating the proposed mechanisms for the nematicity of FeSe, but also points to a unified understanding of the correlation physics⁴² across the seemingly distinct classes of Fe-based superconductors.

Email: luxy@bnu.edu.cn; pdai@rice.edu; Thorsten.schmitt@psi.ch.

References

1. Fradkin, E., Kivelson, S. A. & Tranquada, J. M. Colloquium: theory of intertwined orders in high-temperature superconductors. *Rev. Mod. Phys.* **87**, 457-482 (2015).

2. Chu, J.-H. et al. In-plane resistivity anisotropy in an underdoped iron arsenide superconductor. *Science* **329**, 824-826 (2010).
3. Yi, M. et al. Symmetry-breaking orbital anisotropy observed for detwinned $\text{Ba}(\text{Fe}_{1-x}\text{Co}_x)_2\text{As}_2$ above the spin density wave transition. *Proc. Natl Acad. Sci. USA* **108**, 6878-6883 (2011).
4. Chu, J.-H., Kuo, H.-H., Analytis, J. G. & Fisher, I. R. Divergent nematic susceptibility in an iron arsenide superconductor. *Science* **337**, 710-712 (2012).
5. Fernandes, R. M., Chubukov, A. V. & Schmalian, J. What drives nematic order in iron-based superconductors? *Nat. Phys.* **10**, 97-104 (2014).
6. Si, Q., Yu, R. & Abrahams, E. High temperature superconductivity in iron pnictides and chalcogenides. *Nat. Rev. Mater.* **1**, 16017 (2016).
7. Kuo, H.-H., Chu, J.-H., Palmstrom, J. C., Kivelson, S. A. & Fisher, I. R. Ubiquitous signatures of nematic quantum criticality in optimally doped Fe-based superconductors. *Science* **352**, 958-962 (2016).
8. Böhmer, A. E. & Meingast, C. Electronic nematic susceptibility of iron-based superconductors. *C. R. Phys.* **17**, 90-112 (2016).
9. Böhmer, A. E. & Kreisel, A. Nematicity, magnetism and superconductivity in FeSe. *J. Phys. Condens. Matter* **30**, 023001 (2018).
10. Metlitski, M. A. et al. Cooper pairing in non-Fermi liquids. *Phys. Rev. B* **91**, 115111 (2015).
11. Lederer, S. et al. Enhancement of superconductivity near a nematic quantum critical point. *Phys. Rev. Lett.* **114**, 097001 (2015).
12. Eckberg, C. et al. Sixfold enhancement of superconductivity in a tunable electronic nematic system. *Nat. Phys.* **16**, 346-350 (2020).
13. Hsu, F. C. et al. Superconductivity in the PbO-type structure α -FeSe. *Proc. Natl Acad. Sci. USA* **105**, 14262-14264 (2008).
14. McQueen, T. M. et al. Tetragonal-to-orthorhombic structural phase transition at 90 K in the superconductor $\text{Fe}_{1.01}\text{Se}$. *Phys. Rev. Lett.* **103**, 057002 (2009).
15. Tanatar, M. A. et al. Origin of resistivity anisotropy in the nematic phase of FeSe. *Phys. Rev. Lett.* **117**, 127001 (2016).
16. Coldea, A. & Watson, M. D. The key ingredients of the electronic structure of FeSe. *Annu. Rev. Condens. Matter Phys.* **9**, 125-146 (2018).
17. Liu, D. F. et al. Orbital origin of extremely anisotropic superconducting gap in nematic phase of FeSe superconductor. *Phys. Rev. X* **8**, 031033 (2018).
18. Hashimoto, T. et al. Superconducting gap anisotropy sensitive to nematic domains in FeSe. *Nat. Commun.* **9**, 282 (2018).
19. Rhodes, L. C. et al. Scaling of the superconducting gap with orbital character in FeSe. *Phys. Rev. B* **98**, 180503(R) (2018).
20. Sprau, P. O. et al. Discovery of orbital-selective Cooper pairing in FeSe. *Science* **357**, 75-80 (2017).
21. Lee, C. C., Yin, W.-G. & Ku, W. Ferro-orbital order and strong magnetic anisotropy in the parent compounds of iron-pnictide superconductors. *Phys. Rev. Lett.* **103**, 267001 (2009).
22. Yi, M. et al. The nematic energy scale and the missing electron pocket in FeSe. *Phys. Rev. X* **9**, 041049 (2019).
23. Baek, S.-H. et al. Orbital-driven nematicity in FeSe. *Nat. Mater.* **14**, 210-214 (2015).

24. Böhmer, A. E. et al. Origin of the tetragonal-to-orthorhombic phase transition in FeSe: a combined thermodynamic and NMR study of nematicity. *Phys. Rev. Lett.* **114**, 027001 (2015).
25. Yamakawa, Y., Onari, S. & Kontani, H. Nematicity and magnetism in FeSe and other families of Fe-based superconductors. *Phys. Rev. X* **6**, 021032 (2016).
26. Onari, S., Yamakawa, Y. & Kontani, H. Sign-reversing orbital polarization in the nematic phase of FeSe due to the C_2 symmetry breaking in the self-energy. *Phys. Rev. Lett.* **116**, 227001 (2016).
27. Wang, Q. et al. Strong interplay between stripe spin fluctuations, nematicity and superconductivity in FeSe. *Nat. Mater.* **15**, 159-163 (2016).
28. Wang, Q. et al. Magnetic ground state of FeSe. *Nat. Commun.* **7**, 12182 (2016).
29. Ma, M. W. et al. Prominent role of spin-orbit coupling in FeSe revealed by inelastic neutron scattering. *Phys. Rev. X* **7**, 021025 (2017).
30. Wang, F., Kivelson, S. & Lee, D.-H. Nematicity and quantum paramagnetism in FeSe. *Nat. Phys.* **11**, 959-963 (2015).
31. Yu, R. & Si, Q. Antiferroquadrupolar and Ising-nematic orders of a frustrated bilinear-biquadratic Heisenberg model and implications for the magnetism of FeSe. *Phys. Rev. Lett.* **115**, 116401 (2015).
32. Glasbrenner, J. K. et al. Effect of magnetic frustration on nematicity and superconductivity in iron chalcogenides. *Nat. Phys.* **11**, 953–958 (2015).
33. She, J.-H., Lawler, M. J. & Kim, E.-A. Quantum spin liquid intertwining nematic and superconducting order in FeSe. *Phys. Rev. Lett.* **121**, 237002 (2018).
34. Lu, X. et al. Nematic spin correlations in the tetragonal state of uniaxial-strained $\text{BaFe}_{2-x}\text{Ni}_x\text{As}_2$. *Science* **345**, 657-660 (2014).
35. Chen, T. et al. Anisotropic spin fluctuations in detwinned FeSe. *Nat. Mater.* **18**, 709-716 (2019).
36. Yu, R., Zhu, J.-X. & Si, Q. Orbital-selective superconductivity, gap anisotropy and spin resonance excitations in a multiorbital t - J_1 - J_2 model for iron pnictides. *Phys. Rev. B* **89**, 024509 (2014).
37. Fanfarillo, L. et al. Orbital-dependent Fermi surface shrinking as a fingerprint of nematicity in FeSe. *Phys. Rev. B* **94**, 155138 (2016).
38. Tian, L. et al. Spin fluctuation anisotropy as a probe of orbital-selective hole-electron quasiparticle excitations in detwinned $\text{Ba}(\text{Fe}_{1-x}\text{Co}_x)_2\text{As}_2$. *Phys. Rev. B* **100**, 134509 (2019).
39. Zhou, K. et al. Persistent high-energy spin excitations in iron-pnictide superconductors. *Nat. Commun.* **4**, 1470 (2013).
40. Pelliciari, J. et al. Local and collective magnetism of EuFe_2As_2 . *Phys. Rev. B* **95**, 115152 (2017).
41. Garcia, F. A. et al. Anisotropic magnetic excitations and incipient Néel order in $\text{Ba}(\text{Fe}_{1-x}\text{Mn}_x)_2\text{As}_2$. *Phys. Rev. B* **99**, 115118 (2019).
42. Pelliciari, J. et al. Reciprocity between local moments and collective magnetic excitations in the phase diagram of $\text{BaFe}_2(\text{As}_{1-x}\text{P}_x)_2$. *Commun. Phys.* **2**, 139 (2019).
43. Rahn, M. C. et al. Paramagnon dispersion in β -FeSe observed by Fe L-edge resonant inelastic X-ray scattering. *Phys. Rev. B* **99**, 014505 (2019).
44. Pelliciari, J. et al. Evolution of spin excitations from bulk to monolayer FeSe. *Nat. Commun.* **12**, 3122 (2021).
45. Ament, L. J. P. et al. Resonant inelastic X-ray scattering studies of elementary excitations. *Rev. Mod. Phys.* **83**, 705-767 (2011).

46. Schlappa, J. et al. Spin-orbital separation in the quasi-one-dimensional Mott insulator Sr_2CuO_3 . *Nature* **485**, 82-85 (2012).
47. Peng, Y. Y. et al. Influence of apical oxygen on the extent of in-plane exchange interaction in cuprate superconductors. *Nat. Phys.* **13**, 1201-1206 (2017).
48. Jia, C. et al. Using RIXS to uncover elementary charge and spin excitations. *Phys. Rev. X* **6**, 021020 (2016).
49. Hepting, M. et al. Three-dimensional collective charge excitations in electron-doped copper oxide superconductors. *Nature* **563**, 374-378 (2018).
50. Lu, X. et al. Spin waves in detwinned BaFe_2As_2 . *Phys. Rev. Lett.* **121**, 067002 (2018).
51. Liu, C. et al. Anisotropic magnetic excitations of a frustrated bilinear-biquadratic spin model—implications for spin waves of detwinned iron pnictides. *Phys. Rev. B* **101**, 024510 (2020).
52. Harriger, L. W. et al. Nematic spin fluid in the tetragonal phase of BaFe_2As_2 . *Phys. Rev. B* **84**, 054544 (2011).
53. Wang, M. et al. Doping dependence of spin excitations and its correlations with high-temperature superconductivity in iron pnictides. *Nat. Commun.* **4**, 2874 (2013).
54. Kreisel, A., Andersen, B. M. & Hirschfeld, P. J. Itinerant approach to magnetic neutron scattering of FeSe: effect of orbital selectivity. *Phys. Rev. B* **98**, 214518 (2019).
55. Fernandes, R. M. et al. Iron pnictides and chalcogenides: a new paradigm for superconductivity. *Nature* **601**, 39-44 (2022).
56. Yu, R., Hu, H., Nica, E. M., Zhu, J.-X. & Si, Q. Orbital selectivity in electron correlations and superconducting pairing of iron-based superconductors. *Front. Phys.* **9**, 978347 (2021).
57. Lafuerza, S. et al. Evidence of Mott physics in iron pnictides from X-ray spectroscopy. *Phys. Rev. B* **96**, 045133 (2017).
58. Watson, M. D. et al. Formation of Hubbard-like bands as a fingerprint of strong electron-electron interactions in FeSe. *Phys. Rev. B* **95**, 081106(R) (2017).
59. Evtushinsky, D. V. et al. Direct observation of dispersive lower Hubbard band in iron-based superconductor FeSe. Preprint at <https://arxiv.org/abs/1612.02313> (2016).
60. Ding, W., Yu, R., Si, Q. & Abrahams, E. Effective exchange interactions for bad metals and implications for iron-based superconductors. *Phys. Rev. B* **100**, 235113 (2019).
61. Mukherjee, S., Kreisel, A., Hirschfeld, P. J. & Andersen, B. M. Model of electronic structure and superconductivity in orbitally ordered FeSe. *Phys. Rev. Lett.* **115**, 026402 (2015).
62. Wang, Q. et al. Uniaxial pressure induced stripe order rotation in $\text{La}_{1.88}\text{Sr}_{0.12}\text{CuO}_4$. *Nat. Commun.* **13**, 1795 (2022).
63. Strocov, V. N. et al. High-resolution soft X-ray beamline ADRESS at the Swiss Light Source for resonant inelastic X-ray scattering and angle-resolved photoelectron spectroscopies. *J. Synchrotron Radiat.* **17**, 631-643 (2010).
64. Ghiringhelli, G. et al. SAXES, a high-resolution spectrometer for resonant X-ray emission in the 400-1,600 eV energy range. *Rev. Sci. Instrum.* **77**, 113108 (2006).
65. Lu, X et al. Spin-excitation anisotropy in the nematic state of detwinned FeSe. https://figshare.com/articles/dataset/Spinexcitation_anisotropy_in_the_nematic_state_of_detwinned_FeSe/19382825 (2022).

Methods

Sample preparation. The high-quality BaFe_2As_2 and FeSe single crystals used in the present study were grown using self-flux and the chemical vapour transport method, respectively. The BaFe_2As_2 single crystals were oriented using a Laue camera and cut along the tetragonal $[110]$ and $[1-10]$ directions using a high-precision wire saw (WS-25). The directions of the self-cleaved edges of the FeSe single crystals were also determined using a Laue camera. The well-cut BaFe_2As_2 crystals, with typical dimensions of $5 \text{ mm} \times 4.3 \text{ mm} \times 0.5 \text{ mm}$, were pre-cleaved before the final preparation. For RIXS measurements of BaFe_2As_2 , we placed a ceramic top post onto the upper surface of BaFe_2As_2 for in situ cleaving. For RIXS measurements of FeSe , we glued thin FeSe crystals onto the upper surface of BaFe_2As_2 along the same direction using epoxy Stycast 1266 and a small ceramic top post onto the surface of the FeSe . The prepared crystals with the posts were inserted into the slot of the uniaxial-pressure devices, which were mounted on a modified copper sample holder of the RIXS spectrometer (Fig. 1b)⁶².

Experimental set-ups. The RIXS and XAS measurements were performed with the RIXS spectrometer at the ADRESS beamline of the Swiss Light Source at the Paul Scherrer Institut^{63,64}. The beam size at the sample position was $4 \times 55 \mu\text{m}^2$. All the measurements shown in the main text were collected using linear horizontal (LH) polarization (electric field vector of the incident photons lying within the horizontal scattering plane), denoted as π polarization. The RIXS spectra were collected with a grazing-incidence configuration, as shown in Fig. 1d. The scattering angle was set to $2\theta_s = 130^\circ$, with which a substantial area of the first Brillouin zone is accessible (Fig. 1d, grey circle). The measurements were performed along high-symmetry directions H/K and $[H, H]$ in orthorhombic notation. The total energy resolution for the RIXS measurements was set to 80 meV. The in-plane momentum q_{\parallel} could be tuned continuously by rotating the sample and thereby changing the angle δ . Before the measurements, the sample holder was inserted into the manipulator head and the top post was removed by cleaving at low temperature ($\sim 20 \text{ K}$) and in ultrahigh vacuum ($< 10^{-10} \text{ mbar}$). We defined the wave vector \mathbf{Q} in reciprocal space as $\mathbf{Q} = H\mathbf{a}^* + K\mathbf{b}^* + L\mathbf{c}^*$, where H, K, L are Miller indices and $\mathbf{a}^* = \hat{\mathbf{a}}2\pi/a_o$, $\mathbf{b}^* = \hat{\mathbf{b}}2\pi/b_o$, and $\mathbf{c}^* = 2\pi/c$ are reciprocal lattice unit vectors with $a_o \approx 5.334 \text{ \AA}$, $b_o \approx 5.308 \text{ \AA}$ and $c \approx 5.486 \text{ \AA}$. The FeSe tri-layer height o was $d \approx 5.5 \text{ \AA}$. The orthorhombic lattice s distortion of FeSe was $\delta = (a_o - b_o)/(a_o + b_o) \approx 0.27\%$ at a temperature well below T_s .

Data availability

All data that support the plots in this paper are available from the corresponding author upon reasonable request. Source data are provided with this paper. The data can also be found at Figshare public repository⁶⁵.

Code availability

All relevant source code is available from the corresponding author upon reasonable request.

Acknowledgements

The work at Beijing Normal University is supported by National Key Projects for Research and

Development of China with Grant No. 2021YFA1400400 and the National Natural Science Foundation of China (grants nos. 11922402 and 11734002;) (X.L.). The RIXS experiments were carried out at the ADDRESS beamline of the Swiss Light Source at the Paul Scherrer Institut (PSI). The work at PSI is supported by the Swiss National Science Foundation through project no. 200021_178867 and the Sinergia network Mott Physics Beyond the Heisenberg Model (MPBH; projects nos. CRSII2 160765/1 and CRSII2 141962; T.S.). The work at Renmin University was supported by the Ministry of Science and Technology of China, National Program on Key Research Project grant no. 2016YFA0300504 and Research Funds of Remnin University of China grant no. 18XNLG24 (R.Y.). The experimental work at Rice University is supported by the US Department of Energy, Basic Energy Sciences, under grant no. DE-SC0012311 (P.D.). The single-crystal synthesis work at Rice is supported by the Robert A. Welch Foundation grant no. C-1839 (P.D.). The theoretical work at Rice was supported by the US Department of Energy, Office of Science, Basic Energy Sciences, under award no. DE-SC0018197, and the computational part by the Robert A. Welch Foundation grant no. C-1411 (Q.S.). Q.S. acknowledges the hospitality of the Aspen Center for Physics, which is supported by NSF grant no. PHY-1607611.

Author contributions

X.L. conceived this project and developed the detwinning strategy. X.L. and T.S. wrote the beamtime proposals and coordinated the experiments as well as all other project phases. X.L., W.Z., Y.T., E.P., R.L., Z.T. and T.S. carried out the RIXS experiments with the support of V.N.S. X.L. analysed the data with assistance from Y.S. P.L., R.L. and Z.T. prepared the BaFe₂As₂ single crystals. T.C. and P.D. provided the FeSe single crystals. R.Y. and Q.S. carried out theoretical and computational analyses. X.L., P.D. and T.S. wrote the manuscript with input from R.Y. and Q.S. All authors made comments.

Competing interests

The authors declare no competing interests.

Additional information

Supplementary information The supplementary material is attached at the end of this manuscript.

Correspondence and requests for materials should be addressed to Xingye Lu, Pengcheng Dai or Thorsten Schmitt.

Supplementary information: Spin excitation anisotropy in the nematic state of detwinned FeSe

Xingye Lu,^{*} Wenliang Zhang, Yi Tseng, Ruixian Liu, Zhen Tao, Eugenio Paris, Panpan Liu, Tong Chen, Vladimir N. Strocov, Yu Song, Rong Yu, Qimiao Si, Pengcheng Dai,[†] and Thorsten Schmitt[‡]

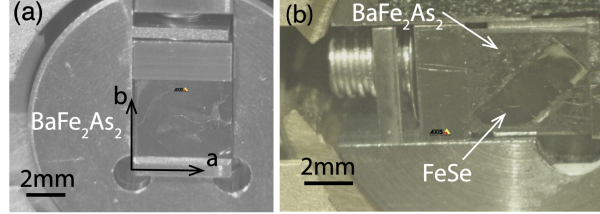


Fig. S1. Mechanical device for detwinning (a) BaFe₂As₂ and (b) FeSe installed on a RIXS sample holder on SAXES spectrometer at ADDRESS beamline, SLS. Uniaxial pressure is applied via tuning the screw on one end. The pressure can be held at low temperature by a Belleville spring washer. A large BaFe₂As₂ crystal (5×4.3×0.4mm³) was inserted into the device in (a) and a FeSe/BaFe₂As₂ sample in (b). Both samples were cleaved at ~ 20 K in high vacuum ($< 1 \times 10^{-8}$ torr).

Spin excitation anisotropy and nematic spin correlations

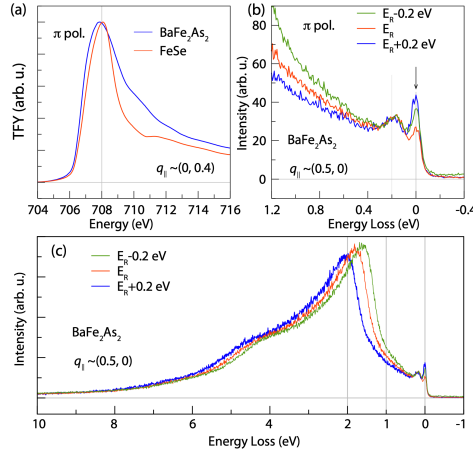


Fig. S2. (a) Comparison of the total fluorescence yield (TFY) XAS spectrum between BaFe₂As₂ (blue curve) and FeSe (red curve). The Fe-L₃ resonance energy (E_R) of FeSe is slightly (~ 0.2 eV) higher than that for BaFe₂As₂. The data were collected at $q_{\parallel} \sim (0, 0.4)$ and $T = 20$ K with π polarization. (b), (c) Brief energy detuning RIXS measurements of detwinned BaFe₂As₂ near the Fe-L₃ edge. The measurements were performed at $T = 20$ K with $q_{\parallel} = (0.5, 0)$. The vertical arrow in (b) marks the E_i -independent spin excitations near the Fe-L₃ edge, indicative of its Raman-mode nature. As a comparison, the fluorescence peak (at $\sim 1.5 - 2$ eV) in (c) shifts to higher energy with increasing E_i .

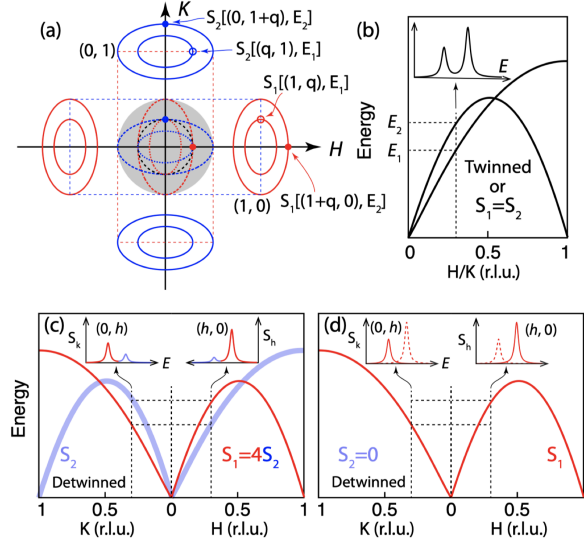


FIG. S3. (a) Reciprocal space and Brillouin zone for typical FeSC systems such as BaFe_2As_2 and FeSe . The red (blue) dashed rectangle are first BZ centering at Γ point associated with $\mathbf{Q}_1 = (1, 0)$ ($\mathbf{Q}_2 = (0, 1)$). The inner (outer) ellipses mark the constant-energy excitations with an energy transfer of E_1 (E_2). (b)-(d) Schematic dispersion for (b) a twinned sample or a sample with no nematic spin correlations ($S_1 = S_2$), (c) a detwinned sample with nematic spin correlations $S_1 > S_2$, and (d) a detwinned sample with S_1 only. The insets in (b)-(d) show the corresponding spectra S_h and S_k .

Figure 3 shows how we can connect the spin-excitation anisotropy measured with RIXS to the intrinsic nematic spin correlations. As we have described in the main text, we define the spin-excitation anisotropy as $\phi(q_{\parallel}) = \frac{\int S_h(q_{\parallel}, E) dE}{\int S_k(q_{\parallel}, E) dE} = S_h(q_{\parallel})/S_k(q_{\parallel})$, in which $S_h(q_{\parallel})$ and $S_k(q_{\parallel})$ are energy integrated spin excitations measured at $(q_{\parallel}, 0)$ and $(0, q_{\parallel})$, respectively. In our previous neutron scattering study, we have defined the nematic spin correlations as $\psi(E) = \frac{S_1(E) - S_2(E)}{S_1(E) + S_2(E)}$ (or $\psi(q, E) = \frac{S_1(q, E) - S_2(q, E)}{S_1(q, E) + S_2(q, E)}$), where $S_{1,2}(E) = \frac{\int S_{1,2}(q, E) dq}{\int dq}$, and the integral $\int dq$ runs over the whole Brillouin zone (BZ). Note q is a reduced momentum within a BZ.

As shown in Fig. S3(a), the RIXS spectra $S_h(q)$ and $S_k(q)$ measured at $(q, 0)$ (red dot) and $(0, q)$ (blue dot) in the first BZ, can be written as:

$$S_h(q) = S_1[(q, 0), E_2] + S_2[(q, 0), E_1] \quad (1)$$

$$S_k(q) = S_1[(0, q), E_1] + S_2[(0, q), E_2] \quad (2)$$

As $S_h(q) > S_k(q)$ at all the momenta measured, the lower limit for $\phi(q)$ is 1, which can be realized in a twinned sample, or a system without nematic spin correlations, as shown in Fig. S3(b). The upper limit for $\phi(q)$ is $S_1[(q, 0), E_2]/S_1[(0, q), E_1]$, which can be achieved in a system where S_2 vanishes, such as the Heisenberg model calculation of the intrinsic spin waves in BaFe_2As_2 [Fig. S3(d)]. Note that

the upper limit could be different in BaFe_2As_2 and FeSe . This could undermine our comparison of the spin-excitation anisotropy between BaFe_2As_2 and FeSe . For a system with nematic state, the spin-excitation anisotropy $\phi(q)$ can reflect the amplitude and energy scale of the nematic spin correlations [Fig. S3(c)].

Fitting of the RIXS spectra

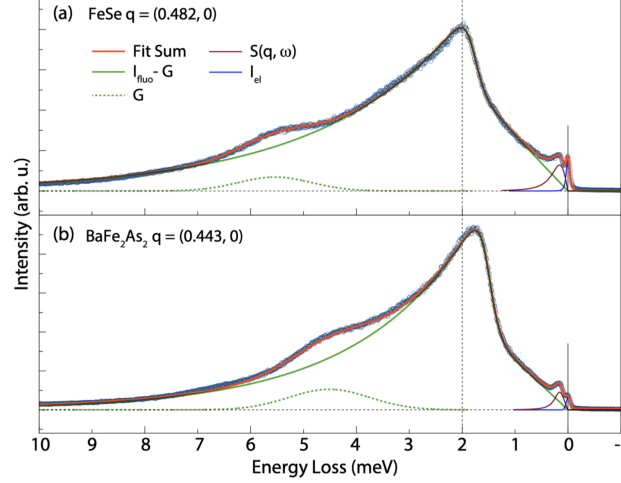


FIG. S4. Fitting of the full RIXS spectra measured at (a) $\mathbf{q}_{\parallel} = (0.482, 0)$ for FeSe , and (b) $\mathbf{q}_{\parallel} = (0.443, 0)$ for BaFe_2As_2 .

To extract the energy dispersion $E(q)$, damping rate, and intensity of the magnetic excitations, we need to use an efficient model to account for the fluorescence (I_{fluo}), (para)magnon ($S(q, E)$) and elastic peak (I_{el}) of RIXS spectra. RIXS spectrum at q can be expressed as:

$$I(E) = I_{\text{fluo}} + S(q, E) + I_{\text{el}} \quad (3)$$

where E is energy transfer (loss), and I_{el} can be described with a resolution-limited gaussian peak. The RIXS spectral weight of iron-based superconductors (FeSC) are usually dominated by strong fluorescence signal at $E \gtrsim 0.5$ eV. Accurate description of fluorescence is important for extracting the magnetic scattering. Previous RIXS studies of FeSC have shown that the fluorescence at $\text{Fe} - L_3$ edge can be well described by the formula:

$$I_{\text{fluo}} = (bE^2 + aE) \cdot (1 - g_{\gamma}) + I_0 \exp(-\alpha E) \cdot g_{\gamma} + G \quad (4)$$

with

$$g_{\gamma} = \left(\exp\left(\frac{E + E^*}{\Gamma}\right) + 1 \right)^{-1} \quad (5)$$

where $G = A_0 \exp\left(\frac{(E+E_s)^2}{2\sigma^2}\right)$ is a gaussian function. g_{γ} generates a smooth crossover from the quasilinear region with $E \lesssim 1$ eV (the first term of Eq. (2)) to the exponential region (the second term of Eq. (4)) [1-3]. As shown in Fig. S4, the overall line-shape of the fluorescence can be well fitted by

Eq. (4). Because the magnetic excitations exist only at low energy ($E \lesssim 0.8\text{eV}$), while the exponential decay dominates the range with much higher energy, we neglect g_γ and describe the low-energy fluorescence using $bE^2 + aE$ in fitting the magnetic excitations.

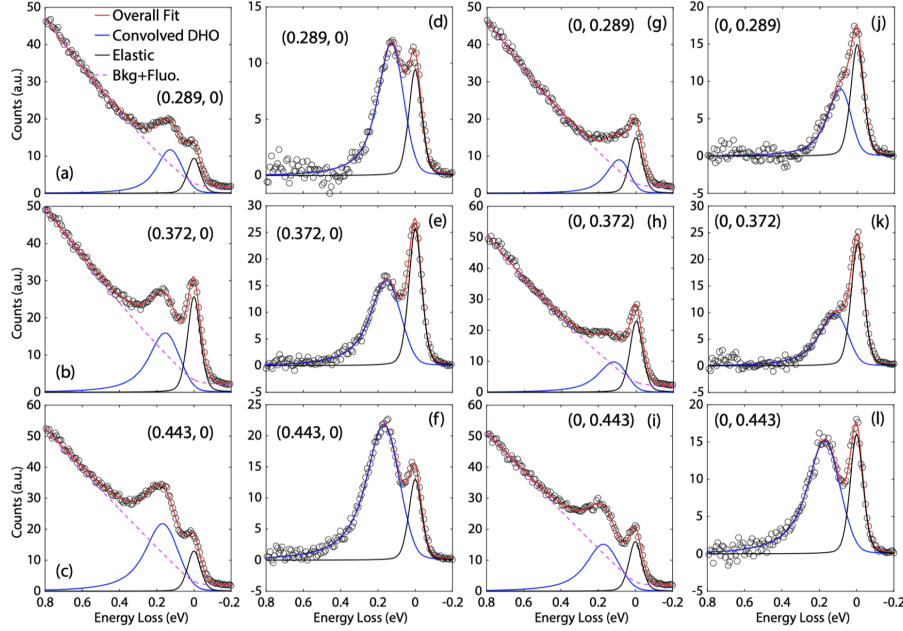


FIG. S5. Selected RIXS spectra along $[H, 0]$ and $[0, K]$ directions for detwinned BaFe_2As_2 and their fittings using the model as described in Eq. (4). Black circles in (a)-(c), (g)-(i) are raw RIXS spectra, and in (d)-(f), (j)-(l) are spectra with fluorescence and background subtracted. Blue curves are a damped harmonic oscillator (DHO) model convolved with an energy-resolution limited gaussian. Black curves are gaussian fittings of the elastic scattering peaks. Pink dashed curves are fluorescence and background. Red curves are the overall fit of the spectra.

Given that the magnetic excitations are heavily damped in itinerant FeSC, we use a general damped harmonic oscillator function to capture the features of the magnetic excitations [4-7]:

$$S(q, E) = A \frac{E_0}{1 - e^{-\beta E}} \frac{2\gamma E}{(E^2 - E_0^2)^2 + (E\gamma)^2}, \quad (6)$$

where β is $\frac{1}{k_B T}$ (k_B is Boltzmann constant). $E_0(q)$ is the undamped energy and $\gamma(q)$ the excitation life time (which represents the damping rate). When the excitations are underdamped ($\gamma/2 < E_0$), we can also describe the spectrum using an antisymmetrized Lorentzian function [5-7],

$$S(q, E) \propto \frac{\gamma/2}{(E - E_q)^2 + (\gamma/2)^2} + \frac{\gamma/2}{(E + E_q)^2 + (\gamma/2)^2}, \quad (7)$$

generating the fitted pole energies $E_q = [E_0^2 - (\gamma/2)^2]^{-1/2}$. In a general case, the undamped energy E_0 and the excitation life time γ are essential information we need to extract from the fitting of the

spectra.

We show in Fig. S4 the overall fitting of the RIXS spectra (blue open circles) using Eq. (4) (red curves), and in Figs. S5 and S6 the fitting of the low-energy magnetic excitations for BaFe_2As_2 and FeSe using Eq. (6). The spectra are well fitted by the damped harmonic oscillator model. The energy dispersions and integrated intensities for BaFe_2As_2 and FeSe have been shown in the main text.

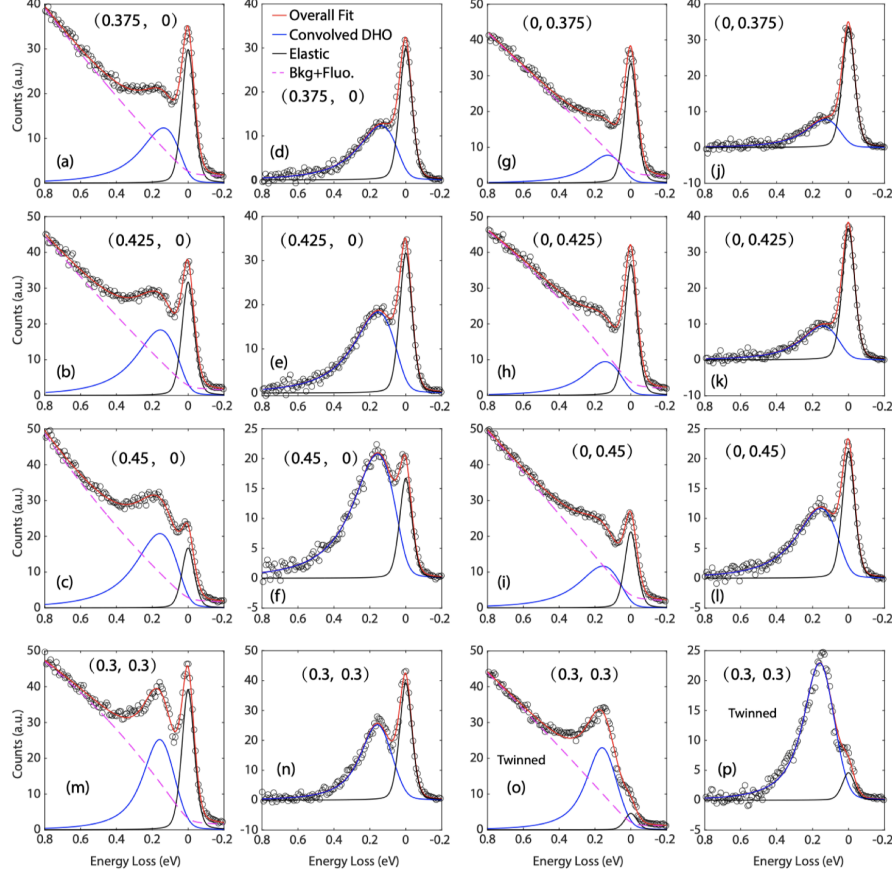


FIG. S6. Fitting of the RIXS spectra of FeSe following the same procedure as that for BaFe_2As_2 in Fig. 3. The spectra in (o) and (p) are measured on twinned sample while the others on detwinned sample.

Theoretical results

Motivated by the dispersive and underdamped feature of the RIXS spectrum in the detwinned FeSe , we study the spin dynamics of an $S = 1$ bilinear-biquadratic Heisenberg model. The Hamiltonian reads

$$H = \frac{1}{2} \sum_{i, \delta_n, \alpha, \beta} \{ J_n S_i \cdot S_j + K_n (S_i \cdot S_j)^2 \}, \quad (8)$$

where $j = i + \delta_n$, and δ_n connects a site i in a square lattice and its n 's nearest neighbor sites with $n = 1, 2, 3$. Here J_n , and K_n are respectively the bilinear and biquadratic couplings between the n 's

nearest neighbor spins. Unlike BaFe₂As₂, the ground state of FeSe is not magnetically ordered but can hold an antiferroquadrupolar (AFQ) order with wave vector $(\pi, 0)$ [8].

Following this, we study the spin dynamics through Schwinger bosons in an $SU(3)$ representation [10]. At each site, we use $|-1\rangle$, $|0\rangle$, and $|1\rangle$ to denote the three eigenstates of the spin operator S^z . They are used for a time-reversal invariant basis of the $SU(3)$ representation:

$$\begin{aligned} |x\rangle &= \frac{i}{\sqrt{2}}(|1\rangle - |-1\rangle), \\ |y\rangle &= \frac{1}{\sqrt{2}}(|1\rangle + |-1\rangle), \\ |z\rangle &= -i|0\rangle. \end{aligned} \quad (9)$$

Within this representation, three Schwinger bosons are associated with the three states, $b_\alpha^\dagger|\emptyset\rangle = |\alpha\rangle$, where $\alpha = x, y, z$, and $|\emptyset\rangle$ is the null state of the Schwinger bosons. The bosons satisfy a local constraint at each site:

$$\sum_\alpha b_{i\alpha}^\dagger b_{i\alpha} = 1 \quad (10)$$

The spin dipolar and quadrupolar operators can be written in terms of the Schwinger boson bilinears as

$$S_i^\alpha = -i\epsilon_{\alpha\beta\gamma}(b_{i\beta}^\dagger b_{i\gamma} - b_{i\gamma}^\dagger b_{i\beta}), \quad (11)$$

$$Q_i^{\alpha\beta} = -(b_{i\alpha}^\dagger b_{i\beta} + b_{i\beta}^\dagger b_{i\alpha}),$$

$$Q_i^{x^2-y^2} = -(b_{ix}^\dagger b_{ix} - b_{iy}^\dagger b_{iy}), \quad (12)$$

$$Q_i^{r^2-3z^2} = \frac{1}{\sqrt{3}}(2b_{iz}^\dagger b_{iz} - b_{ix}^\dagger b_{ix} - b_{iy}^\dagger b_{iy}),$$

where α, β , and γ run over x, y , and z , and $\epsilon_{\alpha\beta\gamma}$ is the Levi-Civita symbol. The Hamiltonian can be rewritten in terms of these Schwinger bosons. The condensation of the boson(s) describes a quadrupolar order. We focus on condensing the b_x and b_y bosons in alternating columns, which specifies the $(\pi, 0)$ AFQ order of the $Q^{x^2-y^2}$ type.

We study the spin excitations in the AFQ phase by using the flavor-wave theory. Referring the detail of the calculation to Ref. [8, 9], here we outline the main results. The transverse dynamical spin structure factor is given as follows:

$$S_D^{xx}(q, \omega) = \frac{1}{2} \sqrt{\frac{A_q + B_q}{A_q - B_q}} \delta(\omega - \epsilon_q), \quad (13)$$

where the magnetic excitation spectrum is

$$\epsilon_q = \sqrt{A_q^2 - B_q^2}, \quad (14)$$

$$A_q = J_1 \cos q_y + J_3 (\cos 2 q_x + \cos 2 q_y) - K_1 - 2K_3, \quad (15)$$

$$B_q = (K_1 - J_1) \cos q_y + (K_3 - J_3) (\cos 2 q_x + \cos 2 q_y). \quad (16)$$

The dispersion of the magnetic excitations for the parameter set $J_1 = J_2 = 10$ meV, $J_3 = -20$ meV, $K_1 = -28$ meV, $K_2 = 48$ meV, and $K_3 = -68$ meV are shown in Fig. 5(a) of the main text. It signals a Goldstone mode at the Brillouin zone center and exhibits anisotropy along the $[H, 0]$ (red line) and $[0, H]$ (blue line) directions. We have made no effort to fine-tune the model parameters, and the theoretical dispersion already provides a good description of the experimental data taking into account the size of the experimental resolution (about 80 meV). Because the dispersion of the transverse excitations does not depend on J_2 and K_2 and also due to the size of the experimental error bar, the model parameters cannot be fully determined by fitting the experimental data.

We further calculate the dynamical spin structure factor along several high symmetric directions of the Brillouin zone. The results along the $[H, 0]$, $[0, H]$, and $[H, H]$ directions are presented in Fig. 5(b) and (c) of the main text. We have adopted a phenomenological damping parameter γ in the calculation, and take $\gamma/2 = 100$ meV, $\gamma/2 = 150$ meV, and $\gamma/2 = 125$ meV along the $[H, 0]$, $[0, H]$, and $[H, H]$ directions, respectively (indicated as the error bars in Fig. 5(a)). By comparing the spectral weights along the $[H, 0]$ and $[0, H]$ directions we find an increasing spectral weight anisotropy with increasing momentum transfer. This anisotropic feature is inherent in the coherence factor of $S_D^{xx}(\mathbf{q}, \omega)$ in Eq. (13).

In summary, we have found that both the spectral weight anisotropy and the dispersion of excitations agree well with experimental results. From this, we can infer that well-defined collective magnetic excitations exist up to about 200 meV in FeSe. The calculated magnetic excitations are associated with the $(\pi, 0)$ AFQ order, which arise from a model of quasi-localized magnetic moments with frustrated exchange interactions. Our results further highlight the important role of strong electron correlations in FeSe and related iron-based superconductors.

References

- [1] Zhou, K. et al., Persistent high-energy spin excitations in iron-pnictide superconductors. *Nat. Commun.* **4**, 1470 (2013).
- [2] Pellicciari et al., Local and collective magnetism of EuFe_2As_2 . *Phys. Rev. B* **95**, 115152 (2017).
- [3] Hancock, J. N. et al., Evidence for core-hole-mediated inelastic x-ray scattering from metallic $\text{Fe}_{1.087}\text{Te}$. *Phys. Rev. B* **82**, 020513(R) (2010).
- [4] Lamsal, J. et al., Extracting paramagnon excitations from resonant inelastic x-ray scattering experiments. *Phys. Rev. B* **93**, 214513 (2016).
- [5] Monney, C. et al., Resonant inelastic x-ray scattering study of the spin and charge excitations in the overdoped superconductor $\text{La}_{1.77}\text{Sr}_{0.23}\text{CuO}_4$. *Phys. Rev. B* **93**, 075103 (2016).
- [6] Peng, Y. Y. et al., Dispersion, damping, and intensity of spin excitations in the monolayer $(\text{Bi, Pb})_2(\text{Sr, La})_2\text{CuO}_{6+\delta}$ cuprate superconductor family. *Phys. Rev. B* **98**, 144507 (2018).

- [7] Rahn, M. C. et al., Paramagnon dispersion in β -FeSe observed by Fe L-edge resonant inelastic x-ray scattering. *Phys. Rev. B* **99**, 014505 (2019).
- [8] Yu, R. & Si, Q., Antiferroquadrupolar and Ising-nematic orders of a frustrated bilinear-biquadratic Heisenberg model and implications for the magnetism of FeSe. *Phys. Rev. Lett.* **115**, 116401 (2015).
- [9] Lai, H.-H., Hu, W. J., Nica, E. M., Yu, Rong & Si, Q., Antiferroquadrupolar order and rotational symmetry breaking in a generalized bilinear-biquadratic model on a square lattice. *Phys. Rev. Lett.* **118**, 176401 (2017).
- [10] Lauchli, A., Mila, F. & Penc, K., Quadrupolar Phases of the $S = 1$ Bilinear-Biquadratic Heisenberg Model on the Triangular Lattice. *Phys. Rev. Lett.* **97**, 087205 (2006)